

Structural Dynamic Analysis of a Space Launch Vehicle using an Axisymmetric Two-dimensional Shell Element

JiSoo Sim*

Korea Aerospace Industries, LTD., 78, Gongdan 1-ro, Sanam-myeon, Sacheon, Gyeongsangnam-do 52529, Republic of Korea

SangGu Lee**

Department of Mechanical and Aerospace Engineering, Seoul National University, Seoul 08826, Republic of Korea

JunBeom Kim***

Republic of Korea Air Force, 221, Gonghang-ro, Dong-gu, Daegu 41052, Republic of Korea

SangJoon Shin****

Department of Mechanical and Aerospace Engineering, Seoul National University, Seoul 08826, Republic of Korea

SeungSoo Park*** and WonSuk Ohm*******

Department of Mechanical Engineering, Yonsei University, 50, Yonsei-ro, Seodaemun-gu, Seoul 03772, Republic of Korea

Abstract

The pogo phenomenon refers to a type of multidiscipline-related instability found in space launch vehicles. It is caused by coupling between the fuselage structure and other structural propulsion components. To predict the pogo phenomenon, it is essential to undertake adequate structural modeling and to understand the characteristics of the feedlines and the propulsion system. To do this, a modal analysis is conducted using axisymmetric two-dimensional shell elements. The analysis is validated using examples of existing launch vehicles. Other applications and further plans for pogo analyses are suggested. In addition, research on the pogo phenomenon of Saturn V and the space shuttle is conducted in order to constitute a pogo stability analysis using the results of the present modal analysis.

Key words: Pogo phenomenon, Structural dynamic analysis, Two-dimensional axisymmetric shell, Rayleigh-ritz method

1. Introduction

Space launch vehicles exhibit many types of multidiscipline-related instabilities caused by coupling between the fuselage structure and other structural subsystem components [1]. These problems are mostly due to coupling between the flight mechanics and flexural modes of a launch vehicle. The buffet phenomenon involves the structural dynamics and the aerodynamics. Longitudinal instability is related to coupling

between the structure and propulsion system. The term 'pogo' has been used in relation to this type of longitudinal instability because its resulting motion resembles that of a pogo stick. This paper primarily investigates the pogo phenomenon of a launch vehicle, which is self-excited longitudinal dynamic instability arising from the interaction between the launch vehicle structure and the propulsion system. It is also one of the most complex problems associated with liquid-propellant launch vehicles. In order to predict the pogo phenomenon

This is an Open Access article distributed under the terms of the Creative Commons Attribution Non-Commercial License (<http://creativecommons.org/licenses/by-nc/3.0/>) which permits unrestricted non-commercial use, distribution, and reproduction in any medium, provided the original work is properly cited.

© * Researcher, Korea Aerospace Industries
** M.S student
*** Researcher, Republic of Korea Air Force
**** Professor, Corresponding author: ssjoon@snu.ac.kr
***** M.S student
***** Professor

accurately, a relevant analysis requires the following elements: a detailed structural dynamics analysis, the characteristics of the feedlines, a propulsion system analysis, and a closed-loop stability analysis. The pogo phenomenon can cause damage to the payload and can harm astronauts and, in the worst cases, can lead to engine failure. This phenomenon has occurred in many launch vehicles. The second reference listed shows a summary of these incidents involving launch vehicles in the United States. Most correspond to the NASA human space flight program during the 1960s which experienced the pogo phenomenon. Thus, it became essential to make accurate predictions of the pogo phenomenon during the development of launch vehicles. Titan II in the Gemini program showed longitudinal vibration at 10–13 Hz for 30 seconds starting ninety seconds after its launch. Such vibration reached its maximum amplitude of $\pm 2.5g$ at approximately 11 Hz. Restraining it below $\pm 0.25g$ was required by NASA [2]. The Saturn V vehicle of the Apollo project also showed pogo instability. AS-502 in 1968 recorded longitudinal vibration of 5 Hz with maximum acceleration of 0.6 g between 105–140 seconds during the first-stage (S-IC) burning process. Longitudinal oscillation was observed in the first two Saturn V manned flights. Finally, a passive pogo suppressor was installed in the space shuttle main engine (SSME).

As mentioned in the previous section, the capability to predict the pogo phenomenon accurately is crucial. A few researchers have investigated the pogo phenomenon since the 1960s. Rubin [3] and Oppenheim [4] developed a comprehensive stability analysis of the pogo phenomenon. A launch vehicle, feedlines, and a propulsion system were idealized using their mathematical models. These models were linear time-invariant models. Pogo stability has also been analyzed using a closed-loop system. The possibility of the pogo phenomenon was examined according to stability of this system. For a more accurate closed-loop pogo stability analysis, it will be necessary to predict the natural vibration characteristics of the structures and feedlines of vehicles.

Many launch vehicles, such as the Delta [5], Atlas [4], Titan, Saturn V [6, 7] types as well as the space shuttle [8, 9] have been analyzed with regard to the pogo phenomenon. An accumulator was considered in Ares I-X in order to suppress the pogo phenomenon [10]. A passive pogo suppressor was applied to these launch vehicles. NASA space vehicle design criteria were also established for the pogo phenomenon [11]. The Ariane series in Europe and H-II in Japan were also subjected to a pogo analysis [13]. Chinese researchers have also studied the pogo phenomenon recently. Zhao et al. [14] conducted a relevant parametric study. Hao et al. [15] analyzed a vehicle structure

using NASTRAN. They also used a rational function and the finite element method to assess the propulsion system. In Korea, similar research was conducted on the KSR-III vehicle [16].

In order to predict the pogo phenomenon, knowledge of the structural dynamic characteristics of the launch vehicle is essential. Therefore, this paper concentrates on a structural analysis of a launch vehicle as part of an overall stability analysis of the pogo phenomenon. There have been numerous modal analyses and experiments conducted on launch vehicles. For efficient structural modeling, one-dimensional modeling has been available since the 1960s and 70s using lumped masses and one-dimensional springs. This methodology has been published in many NASA documents [17, 18] involving a range of criteria [19, 20]. Kim et al. developed a method for the one-dimensional modeling of a space launch vehicle [21]. In their attempt, the interaction between the tanks and the liquid propellants was highlighted, specifically the hydroelastic effect. Because the characteristics of the tank component were significantly influential, it was necessary to reflect the hydroelastic effect correctly in the one-dimensional model.

Two- and three-dimensional models have been considered for more accurate analyses. Archer et al. [22, 23] developed a structural modeling method using a two-dimensional axisymmetric shell. Previously, the Saturn V vehicle and the space shuttle [24] were modeled using NASTRAN. Comparisons of the natural frequencies and mode shapes between the analyses and experiments were also done.

This paper will attempt to establish an improved process for predicting the pogo phenomenon. For this purpose, a modal analysis of a complete space launch vehicle will be conducted. For an accurate modal analysis, an improved structural model will be developed. Two-dimensional modeling will be considered to improve the current one-dimensional model [25, 26]. In more detail, the paper will adopt a two-dimensional axisymmetric shell element. The hydroelastic effect will also be considered. A relevant computer program will be developed and validated using a sample launch vehicle. Structural dynamic characteristics will be obtained through a modal analysis of the space launch vehicle.

In addition to the structural dynamic analysis, a pogo stability analysis will be conducted. Because documents pertaining to the Saturn V vehicle and the space shuttle with regard to the pogo phenomenon are available, analyses will be conducted on those two vehicles. Ultimately, this paper will contribute to the realization of improved pogo stability analyses.

2. Pogo Stability Analysis

2.1 Simplified Pogo Analysis of Saturn V

Pogo phenomenon analyses were developed and conducted on the Saturn V vehicle and the space shuttle. Fundamentally, the pogo phenomenon is analyzed using two transfer functions in a closed-loop system. The first of these is related to the structural system, $G(s)$, and the second is linked to the propulsion system, $H(s)$, as shown in Fig. 1. Therefore, $G(s)$ and $H(s)$ should reflect the characteristics of a realistic system accurately. Such a closed system will be analyzed under a certain flight condition in which the pogo phenomenon could arise. Finally, the pogo phenomenon will be predicted according to the stability of the closed-loop system.

A pogo stability investigation of the Saturn V vehicle was conducted by Sterett et al. [6]. They provided a complete summary of the evolution of the pogo analysis methodology. They analyzed the second stage, S-II, and the third stage, S-IVB, as well as the first stage, S-IC. In addition, von Pragenau [7] suggested a simplified pogo closed-loop analysis, as shown in Fig. 2. This diagram illustrates a system

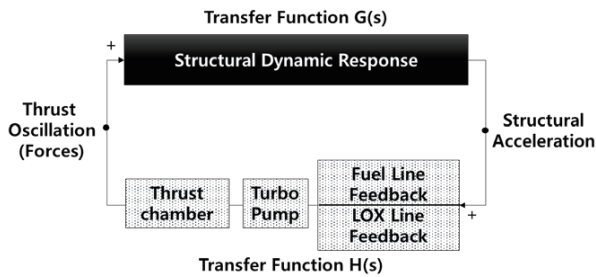


Fig. 1. Closed loop system of the pogo phenomenon

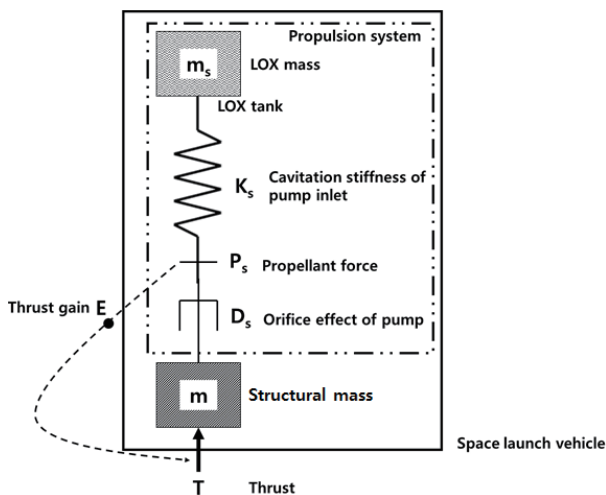


Fig. 2. Simplified pogo closed loop analysis

consisting of both a LOX tank and a thrust chamber among several supply/propulsion components in a launch vehicle. In his result, the relationships among the propellant force P_s , the constant gain E , the thrust T , the force F_s , the cavitation stiffness K_s , the orifice effect of the pump D_s , and the disturbance force f were obtained. The thrust T was caused by the propellant force P_s , and the force F_s was defined as the sum of the thrust and the disturbance force f . These are expressed in Eqs. (1) and (2).

$$P_s \cdot E = T, \quad (1)$$

$$F_s = P_s \cdot E + f. \quad (2)$$

In the structural model including the orifice effect, cavitation, and propellant, the propellant force P_s was related to the force F_s . The relevant expression among the system, the propellant force, is given in Eq. (3). All of these equations utilize the Laplace transform.

$$P_s = \frac{F_s}{1 + \frac{m}{m_s} + s \frac{m}{D_s} + s^2 \frac{m}{K_s}}. \quad (3)$$

The closed-loop system equation will become complete by combining Eqs. (2) and (3). The resulting equation can then be written as follows:

$$P_s = \frac{f}{1 + \frac{m}{m_s} - E + s \frac{m}{D_s} + s^2 \frac{m}{K_s}}. \quad (4)$$

Finally, the stability will be determined by the sign of the eigenvalues s . Such a determination criterion is expressed in Eq. (5).

$$E < 1 + \frac{m}{m_s}. \quad (5)$$

This complete relationship of the closed-loop system is illustrated by the block diagram shown in Fig. 3. This result represents a simplified but complete process of analyzing the pogo phenomenon.

2.2 Pogo Suppression in the Space Shuttle

For the space shuttle, a relevant pogo integration panel was organized by various NASA research centers and contractors [8]. As a result, a passive pogo suppressor was developed and installed, although both passive and active devices were investigated simultaneously. The relevant analytical model and the methodology used were quite systematic. Owing to the specific configuration of the space shuttle, with an external tank, a feedline of a significant length (31 m) was designed and adopted. Liquid oxygen is significantly heavier than liquid hydrogen, which is the main fuel of the

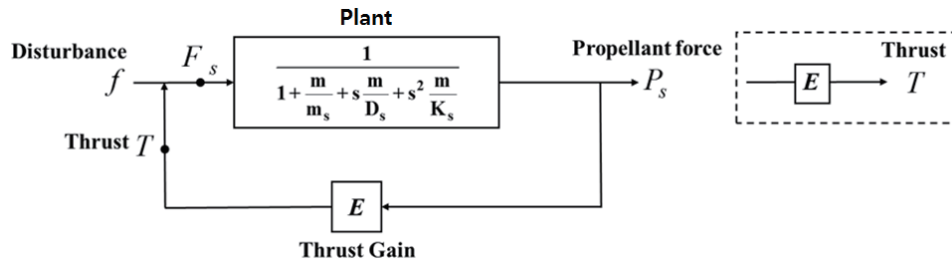


Fig. 3. Block diagram of a simplified pogo analysis

space shuttle. Therefore, the analytical model of the space shuttle was composed of a LOX tank, a longitudinal lateral feedline, a low and high LOX pump, and a chamber [9], as shown in Fig. 4. A few specific flight conditions, i.e., the lift off, maximum dynamic pressure (max. Q), the condition before solid rocket booster (SRB) jettison, and that after SRB jettison, all prone to pogo instability, were selected and analyzed. The analytical model used was composed of 14 variables for the propulsion system. The variables consisted of the generalized coordinates of the fuselage, q_n , the pressures of two thrust chamber points, P , and the flow rates of the tank outlet to eight points, Q , as listed in Eq. (6). In the generalized coordinates of the fuselage, q_n , subscript n denotes the n -th mode of the fuselage.

$$\hat{H} = \{P_2, P_4, P_5, P_7, P_8, P_c, Q_1, Q_2, Q_3, Q_4, Q_5, Q_7, Q_8, q_n\}, \quad (6)$$

$$\{[V(s)] + [E][F(s)]\} \cdot \hat{H} = 0. \quad (7)$$

The complete system became a 14-order variable system, as expressed by Eq. (7). $[V(s)]$ is the complete system, composed of both structural and propulsion state variables. $[E]$ is the position of the pogo suppressor. $[F(s)]$ denotes the characteristics of the pogo suppressor. Pogo instability was examined through an eigenvalue analysis of the system.

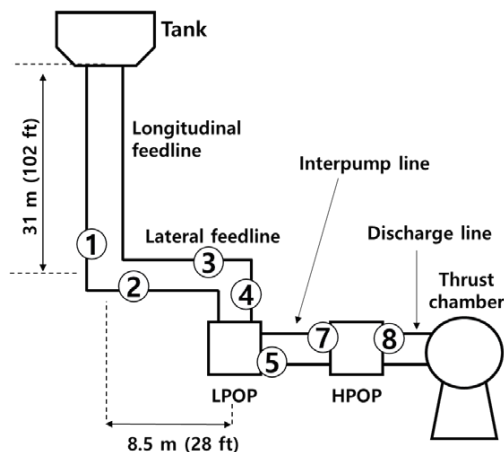


Fig. 4. Pogo analysis of the example space shuttle

This was done by employing several structural modes of each flight condition and varying the natural frequencies by $\pm 15\%$. Pogo instability occurred when the damping ratio decreased significantly and became negative. This analysis procedure suggested what would be required for formulating the pogo analysis. The first variables needed would be the characteristics of the structural system in terms of the generalized coordinates, here represented by q . The second would be an analytical model of the feedlines and propulsion system in terms of the pressures and flow rates. The relationship between the structural system q and the propulsion system P and Q would also be needed.

3. Structural Modeling and Modal Analysis

3.1 Modal Analysis of the Launch Vehicles

This section focuses on the structural dynamic response of a launch vehicle. The transfer function $G(s)$ will be required to predict the response. $G(s)$ is referred to as “the plant” in Fig. 3. The transfer function $G(s)$ refers to the natural frequencies and mode shapes of the launch vehicle. A modal analysis will be conducted to determine the transfer function $G(s)$ via an appropriate structural model. The modal analysis proceeds as follows. Assuming that the launch vehicle is an undamped system, mass and stiffness matrices are used in the modal analysis. These are expressed by Eq. (8).

$$[M]\{\ddot{x}\} + [K]\{x\} = 0, \quad (8)$$

$$\omega_n^2 [M]\{x\} + [K]\{x\} = 0, \quad (9)$$

$$\omega_n^2 \{x\} = -[K][M]^{-1}\{x\}. \quad (10)$$

Equation (8) can be rearranged to become Eq. (10). Equation (10) is an eigenvalue problem. When the eigenvalue problem is solved, the eigenvalues will become the natural frequencies and the eigenvectors will become the mode shapes. Equation (11) is a generalized form using the natural frequencies and mode shapes ϕ . Then, by dividing the left-

hand side of Equation (11) by $[M][\phi]$, the second-order differential equation for ξ can be simplified. This is expressed as Equation (12). Equation (13) shows the situation when the resultant force (excitation) exists. It is expressed in terms of the generalized coordinates, and $\{\xi\}$ denotes the modal displacement.

$$[M][\phi]\{\ddot{\xi}\} + [K][\phi]\{\xi\} = 0, \quad (11)$$

$$\{\ddot{\xi}\} + [\Omega]\{\xi\} = 0, \quad (12)$$

$$\{\xi\} + [\Omega]\{\xi\} = [\phi]^T [F]. \quad (13)$$

When Eqs. (12) and (13) are obtained, the transfer function $G(s)$ will be constructed.

3.2 Structural Modeling of a Complete Launch Vehicle

Structural modeling is the first step of a modal analysis. Structural modeling is done to obtain the mass and stiffness matrices of the launch vehicle in this case. Structural modeling methodologies can be categorized according to the dimensions of the structural elements used. In this paper, a two-dimensional shell element is used specifically for the structural modeling step. In more detail, such an element is termed a two-dimensional axisymmetric shell element. Archer and Rubin [22] introduced this methodology, after which the relevant software was developed. The purpose of the software was to predict the structural dynamics of an axisymmetric launch vehicle while focusing on the longitudinal direction. This paper adopts a similar methodology, as defined below.

The liquid-propellant launch vehicle is composed of the payload, a tank, the propellant, the engine, instruments, and the external shells. The characteristics of each component are discussed below. In this approach, a launch vehicle will be disassembled into the following three components:

the spring-mass component, the shell component, and the fluid component. The spring-mass component is a lumped mass and a one-dimensional massless spring. This element is identical to that used in the conventional one-dimensional structural modeling approach. The payload, engine, and instruments are modelled by spring-mass components that are heavy and exhibit little influence upon the fuselage. Tanks and external shells are modelled using shell components. These components account for most of the structure in the launch vehicle. They also contribute to the creation of the mass and stiffness matrices. The detailed mathematical procedure is based on the Rayleigh-Ritz method. The shell elements have longitudinal, radial, and rotational coordinates, and they are divided into the upper elliptical bulkhead, the lower elliptical bulkhead, and a conical shell in accordance with the geometry of the shell. A fluid component is used to represent the liquid propellant. The fluid component has coordinates identical to those of the shell element, creating, however, only a mass matrix. Therefore, when under vibratory motion, the effect of the fluid mass matrix will be added to the structural shell element. Additionally, the motion of the shell element and that of the fluid will become identical. The fluid component is surrounded by the following three shell elements: the upper bulkhead, the conical shell, and the lower bulkhead. This element does not create additional degrees of freedom, as does the virtual mass in NASTRAN. The complete procedure is illustrated in Fig. 5.

3.3 Formulation

The implementation procedure for the formulation of the shell element is conducted using the Rayleigh-Ritz method based on polynomial functions. The displacements of an individual shell component are expressed in Eqs. (14) and (15).

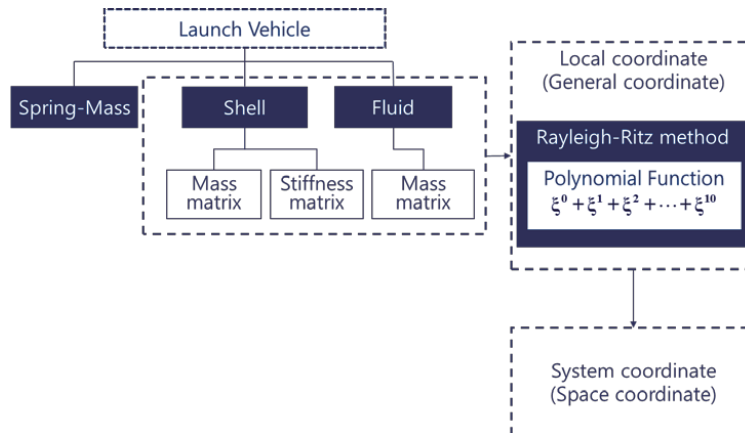


Fig. 5. Structural modeling of a launch vehicle using two-dimensional shell elements

$$u(\xi) = \sum_{k=1}^{\bar{U}} \bar{\alpha}_k u_k(\xi) \quad (14)$$

$$v(\xi) = \sum_{l=1}^{\bar{V}} \bar{\beta}_l v_l(\xi) \quad (15)$$

$$u_k(\xi) = \sum_{n=0}^{10} a_{kn} \xi^n, \quad v_l(\xi) = \sum_{n=0}^{10} b_{ln} \xi^n \quad (16)$$

The displacements of the shell and the direction of the $u(\xi)$ and $v(\xi)$ coordinates are shown in Fig. 6. Equation (16) is the formulation of a mode shape using the polynomial functions. a_{kn} and b_{ln} are arbitrarily specified coefficients, and ξ is a dimensionless variable corresponding to the geometry of the shell. This variable can be described under the following three categories: the conical shell, the upper bulkhead, and the lower bulkhead, as shown in Fig. 7. The upper and lower bulkheads are ellipsoidal shell elements.

$$\xi = \frac{s}{L} \sin \phi_0 \quad (17)$$

$$\xi = \frac{\phi}{\phi_0} \quad (18)$$

$$\xi = \frac{\pi - \phi}{\pi - \phi_0} \quad (19)$$

Equations (17), (18), and (19) are the dimensionless variables of the conical shell, upper bulkhead, and lower bulkhead. The shell stiffness and mass matrices are shown in Eqs. (20) and (21), respectively.

$$[K] = \begin{bmatrix} \frac{\partial^2 V}{\partial \bar{\alpha}_1 \partial \bar{\alpha}_1} & \dots & \frac{\partial^2 V}{\partial \bar{\alpha}_1 \partial \bar{\alpha}_{\bar{U}}} & \frac{\partial^2 V}{\partial \bar{\alpha}_1 \partial \bar{\beta}_1} & \dots & \frac{\partial^2 V}{\partial \bar{\alpha}_1 \partial \bar{\beta}_{\bar{V}}} \\ \frac{\partial^2 V}{\partial \bar{\alpha}_{\bar{U}} \partial \bar{\alpha}_1} & \dots & \frac{\partial^2 V}{\partial \bar{\alpha}_{\bar{U}} \partial \bar{\alpha}_{\bar{U}}} & \frac{\partial^2 V}{\partial \bar{\alpha}_{\bar{U}} \partial \bar{\beta}_1} & \dots & \frac{\partial^2 V}{\partial \bar{\alpha}_{\bar{U}} \partial \bar{\beta}_{\bar{V}}} \\ \frac{\partial^2 V}{\partial \bar{\beta}_1 \partial \bar{\alpha}_1} & \dots & \frac{\partial^2 V}{\partial \bar{\beta}_1 \partial \bar{\alpha}_{\bar{U}}} & \frac{\partial^2 V}{\partial \bar{\beta}_1 \partial \bar{\beta}_1} & \dots & \frac{\partial^2 V}{\partial \bar{\beta}_1 \partial \bar{\beta}_{\bar{V}}} \\ \frac{\partial^2 V}{\partial \bar{\beta}_{\bar{V}} \partial \bar{\alpha}_1} & \dots & \frac{\partial^2 V}{\partial \bar{\beta}_{\bar{V}} \partial \bar{\alpha}_{\bar{U}}} & \frac{\partial^2 V}{\partial \bar{\beta}_{\bar{V}} \partial \bar{\beta}_1} & \dots & \frac{\partial^2 V}{\partial \bar{\beta}_{\bar{V}} \partial \bar{\beta}_{\bar{V}}} \end{bmatrix} \quad (20)$$

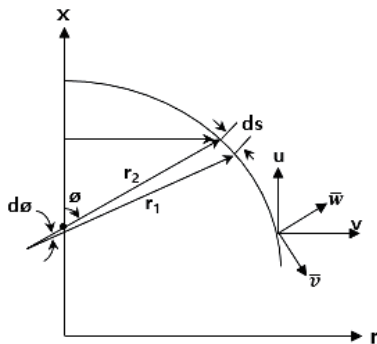


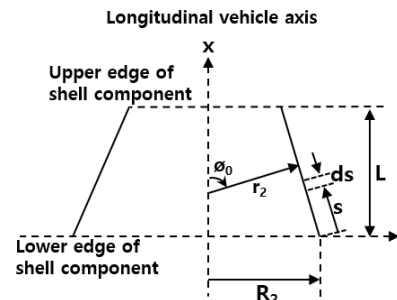
Fig. 6. Coordinates of the shell elements

$$[M] = \begin{bmatrix} \frac{\partial^2 T}{\partial \bar{\alpha}_1 \partial \bar{\alpha}_1} & \dots & \frac{\partial^2 T}{\partial \bar{\alpha}_1 \partial \bar{\alpha}_{\bar{U}}} & \frac{\partial^2 V}{\partial \bar{\alpha}_1 \partial \bar{\beta}_1} & \dots & \frac{\partial^2 V}{\partial \bar{\alpha}_1 \partial \bar{\beta}_{\bar{V}}} \\ \frac{\partial^2 T}{\partial \bar{\alpha}_{\bar{U}} \partial \bar{\alpha}_1} & \dots & \frac{\partial^2 T}{\partial \bar{\alpha}_{\bar{U}} \partial \bar{\alpha}_{\bar{U}}} & \frac{\partial^2 V}{\partial \bar{\alpha}_{\bar{U}} \partial \bar{\beta}_1} & \dots & \frac{\partial^2 V}{\partial \bar{\alpha}_{\bar{U}} \partial \bar{\beta}_{\bar{V}}} \\ \frac{\partial^2 V}{\partial \bar{\beta}_1 \partial \bar{\alpha}_1} & \dots & \frac{\partial^2 V}{\partial \bar{\beta}_1 \partial \bar{\alpha}_{\bar{U}}} & \frac{\partial^2 T}{\partial \bar{\beta}_1 \partial \bar{\beta}_1} & \dots & \frac{\partial^2 T}{\partial \bar{\beta}_1 \partial \bar{\beta}_{\bar{V}}} \\ \frac{\partial^2 V}{\partial \bar{\beta}_{\bar{V}} \partial \bar{\alpha}_1} & \dots & \frac{\partial^2 V}{\partial \bar{\beta}_{\bar{V}} \partial \bar{\alpha}_{\bar{U}}} & \frac{\partial^2 T}{\partial \bar{\beta}_{\bar{V}} \partial \bar{\beta}_1} & \dots & \frac{\partial^2 T}{\partial \bar{\beta}_{\bar{V}} \partial \bar{\beta}_{\bar{V}}} \end{bmatrix} \quad (21)$$

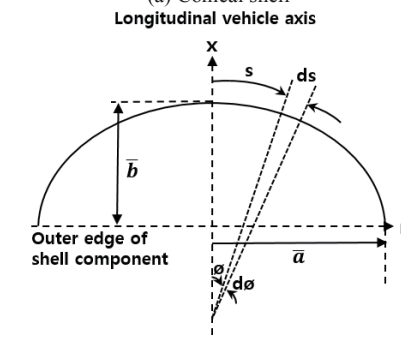
V and T are the potential and kinetic energy, respectively. The coordinate used in the modeling of the shell component is shown in Fig. 6.

$$V = \frac{1}{2} \int_s 2\pi r \left(N_\phi \varepsilon_\phi + N_\theta \varepsilon_\theta + M_\phi K_\phi + M_\theta K_\theta + N_\phi^o \rho^2 \right) ds \quad (22)$$

$$\frac{\partial^2 V}{\partial \bar{\alpha}_k \partial \bar{\beta}_l} = 2\pi \int_s r \left\{ \begin{aligned} & \left[C_{11} \frac{\partial \varepsilon_\phi}{\partial \bar{\alpha}_k} + C_{12} \frac{\partial \varepsilon_\theta}{\partial \bar{\alpha}_k} \right] \frac{\partial \varepsilon_\phi}{\partial \bar{\beta}_l} \\ & + \left[C_{12} \frac{\partial \varepsilon_\phi}{\partial \bar{\alpha}_k} + C_{22} \frac{\partial \varepsilon_\theta}{\partial \bar{\alpha}_k} \right] \frac{\partial \varepsilon_\theta}{\partial \bar{\beta}_l} \\ & + \left[C_{33} \frac{\partial K_\phi}{\partial \bar{\alpha}_k} + C_{34} \frac{\partial K_\theta}{\partial \bar{\alpha}_k} \right] \frac{\partial K_\phi}{\partial \bar{\beta}_l} \\ & + \left[C_{34} \frac{\partial K_\phi}{\partial \bar{\alpha}_k} + C_{44} \frac{\partial K_\theta}{\partial \bar{\alpha}_k} \right] \frac{\partial K_\theta}{\partial \bar{\beta}_l} \\ & + N_\phi^o \frac{\partial \rho}{\partial \bar{\alpha}_k} \frac{\partial \rho}{\partial \bar{\beta}_l} \end{aligned} \right\} ds \quad (23)$$



(a) Conical shell



(b) Ellipsoidal shell

Fig. 7. Geometry of the shell element

Each elemental stiffness matrix is formulated in Eq. (23); the potential energy is given by Eq. (22). On the right-hand side of Eq. (22), ε_ϕ , ε_θ denotes the strain, K_ϕ , K_θ represents the curvature, and ρ is the meridional rotation. Finally, N_ϕ^0 is the initial meridional stress. In an orthotropic shell, N_ϕ , N_θ , M_ϕ , N_θ all refer to the stress in the meridional directions and principal directions in the hoop [22]. C_{11} , C_{12} , C_{22} , C_{33} , C_{34} , and C_{44} are the orthotropic stress-strain and orthotropic moment-curvature coefficients. Finally, the elemental stiffness and mass matrices are obtained by Eqs. (24) and (25), respectively. K_1 , K_2 , ..., and K_{13} are the approximate analytical coefficients.

$$[K] = 2\pi \int r \begin{pmatrix} \int r (K_1 \cdot \{u\} \cdot \{u\}^T + K_2 \cdot \{u\} \cdot \{u\}^T \\ + K_3 \cdot \{u\} \cdot \{u\}^T + \{u\} \cdot \{u\}^T \\ + K_4 \cdot \{v\} \cdot \{v\}^T + \{v\} \cdot \{v\}^T \\ + \dots + K_{13} \cdot \{u\} \cdot \{u\}^T + \{u\} \cdot \{v\}^T) \end{pmatrix} r_1 d\phi \quad (24)$$

$$[M] = 2\pi \int r (\{u\} \cdot \{u\}^T + \{v\} \cdot \{v\}^T) ds \quad (25)$$

The fluid component provides only the mass matrix. The fluid motion is expressed as a function of the generalized displacements of the shell components. The fluid motion and coordinates are shown in Fig. 8. The mass matrix of the fluid component is determined by Eq. (26). The fluid is assumed to be incompressible and inviscid. $\hat{u}_m(x)$ is equal to the change in volume below a given location x divided by the corresponding tank cross-sectional area. The radial fluid motion varies linearly with the spatial coordinate.

$$[M] = 2\pi \gamma_b \int_{-\bar{H}_1}^H \int_0^r \hat{r} (\{\hat{u}(x)\} \cdot \{\hat{u}(x)\}^T + \{\hat{v}(x, \hat{r})\} \cdot \{\hat{v}(x, \hat{r})\}^T) d\hat{r} dx \quad (26)$$

Each component of the shell and fluid is estimated to provide the mass and stiffness matrices. These matrices are described in the local coordinates (generalized coordinates)

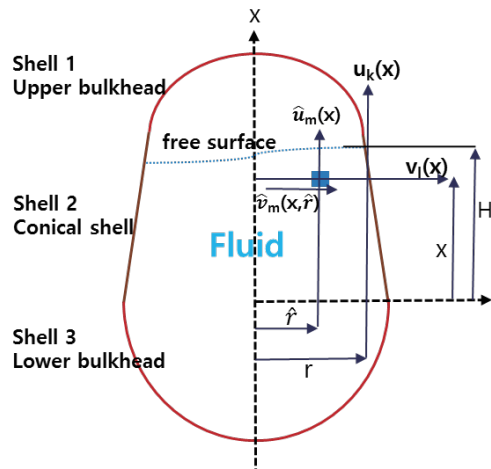


Fig. 8. Definition of the fluid motion

shown in Fig. 5. These matrices can be transformed into the system coordinates (spatial coordinates). As a result, all of the components are combined to provide one mass and one stiffness matrix.

4. Numerical Results and Discussion

4.1 Construction of the Present Analysis

The present analysis is developed using the methodology explained in the previous sections. MATLAB is used for the baseline program. The variable 'sym' is used to represent the symbolic variables for the normalized variable when it changes from 0 to 1. The function 'int' is used to express the definite integral for the matrix element. The eigenvalue problem is solved by the function 'eig'. The present numerical integration is conducted using a variable size in steps for enhanced accuracy instead of the 16-point Gaussian weighting methodology described in the literature (Ref. 22).

4.2 Validation using a Sample Launch Vehicle

The example input and output were sourced from the literature (Refs. 22 and 23). The present example is a single-stage liquid launch vehicle that is axisymmetric, as shown in Fig. 9 (a). A further structural model of the example is shown in Fig. 9 (b). This model is composed of 11 shell components, four spring-mass components, and two fluid components and thus has a total of 30 degrees of freedom. The four spring-mass elements are used to represent the payload, equipment, and engine. The two fluid components serve to represent the oxidizer and the fuel. The mass and stiffness matrices are compared for each element against the existing analytical prediction included in Ref. 22. The difference for each element is less than 2%. Finally, mass and stiffness matrices of 30 30 are obtained for the present example launch vehicle. The eigenvalue problem is solved using these matrices. The natural frequencies are then obtained by the present program.

The results for the mode shape by the present analysis are shown in Figs. 10(a) and 11. The relevant two-dimensional model uses 30 coordinates. These coordinates are composed of those in the longitudinal, radial, and rotational directions. Among these, only the longitudinal direction coordinates are used to show the relevant mode shapes. In Fig. 10(b), the red line designates the mode shape of the complete launch vehicle. The red star represents the coordinates of the tanks. There are a few points outside of the line because bulkheads exist inside a launch vehicle.

The three-dimensional NASTRAN eigenanalysis results

are compared in order to highlight the validation of the present analysis. The three-dimensional NASTRAN analysis configuration is shown in Fig. 12. In it, the example launch vehicle is constructed using the shell elements, and the fluid contained inside the tank is modeled as a lumped mass matrix. The total number of elements and nodes used in NASTRAN modeling are 3,600 and 3,525, respectively. Moreover, there exists no restriction on the degrees of freedom in the boundary location because the launch vehicle is in a free-free condition. Thus, the total number of degrees of freedom used by NASTRAN reaches 21,150 because six degrees of freedom are used per node (translation, rotation

along the x, y, and z coordinate). Given that in total there are 30 degrees of freedom used in the present analysis, there are thus 705 times as many degrees of freedom in the NASTRAN analysis. Therefore, it can be concluded that the present analysis is capable of providing accurate predictions of the axial dynamic characteristics of a launch vehicle while requiring far fewer computational resources.

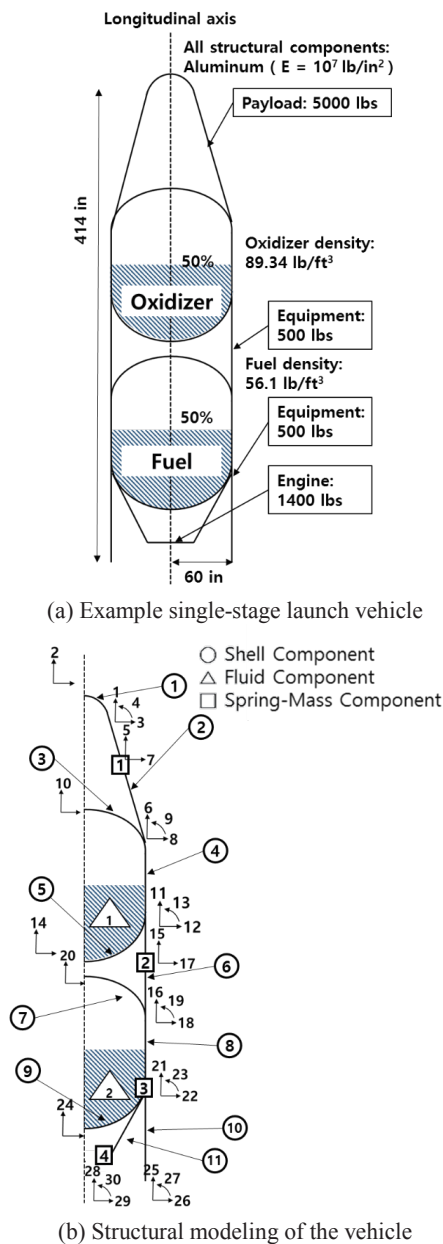


Fig. 9. Example single-stage launch vehicle

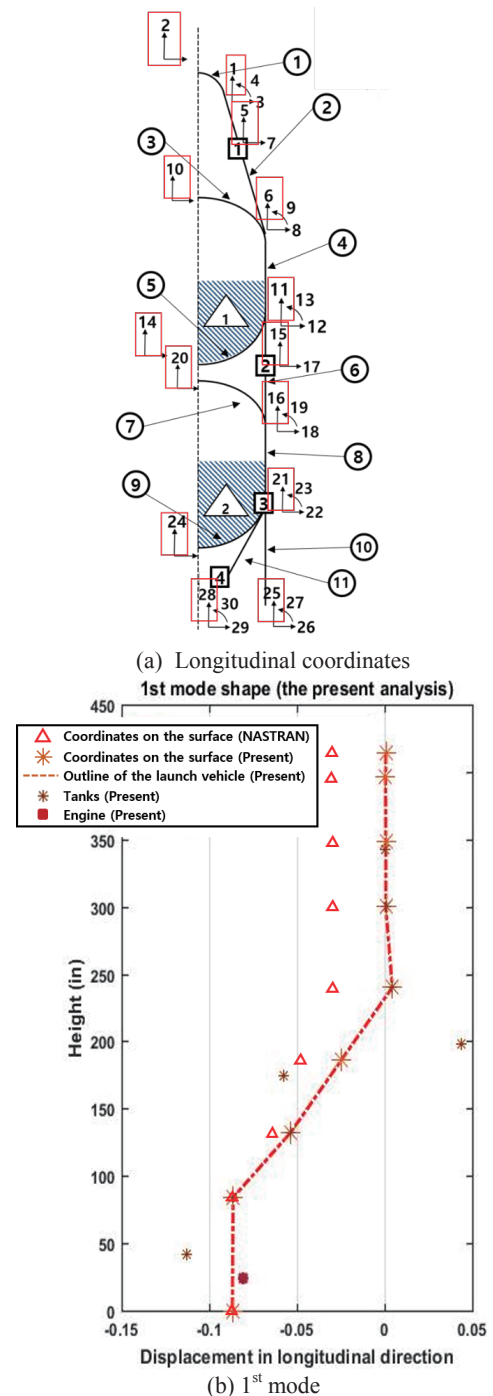


Fig. 10. Comparison of the first mode shape of the example launch vehicle

Table 1 shows the comparison results up to the ninth axial mode. The discrepancy between the present and the NASTRAN analysis result was found to be as low as 0.7%. And, relatively large differences are found for the first and third modes. This is because both results have different number of degrees of freedom per node. Three-dimensional NASTRAN results describe the radial motions by using six degrees of freedom in the longitudinal direction. On the contrary, the present analysis expresses only an axial motion in the

longitudinal direction. Fig. 10 also shows the mode shapes derived from the present analysis and NASTRAN. In Fig. 10 (b), the three-dimensional analysis results are illustrated which correspond to the coordinates included in the surface of the present analysis. A comparison of the two sets of results shows that the results of the overall prediction are similar. Fig. 11 shows additional mode shapes corresponding to the second to the ninth mode as predicted by NASTRAN. And, the first and third mode shapes are also in good agreement.

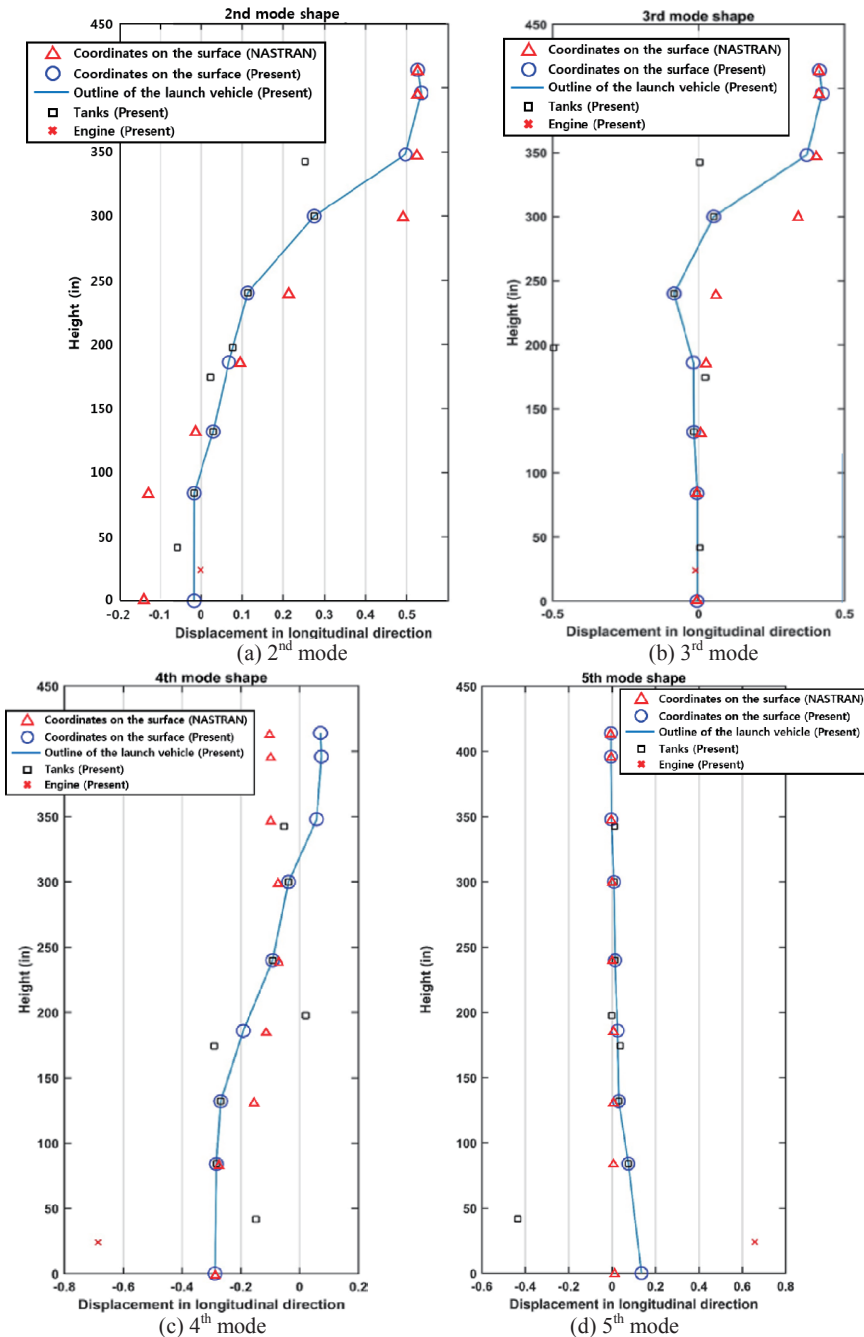


Fig. 11. Comparison of the 2nd~9th mode shapes of the example launch vehicle

Therefore, both predictions give similar results regarding the axial natural frequencies of the example launch vehicle.

It was also found that the pressure change caused by the structural response at the bottom of the tanks will be important for accurate predictions of the pogo phenomenon. Such a change brings about variation of the pressures and the flow rates of the feedlines. As a result, the thrust will also change due to the pressure variation at the bottom of

the tank. For the example of the single-stage launch vehicle, the fourteenth degree of freedom is assigned to the bottom of the LOX tank. Therefore, changing the pressure can be done after analyzing the response of the fourteenth degree of freedom relative to the response of the complete launch vehicle. This pressure change will finally be estimated using the relationship between the structural acceleration and the pressure disturbance.

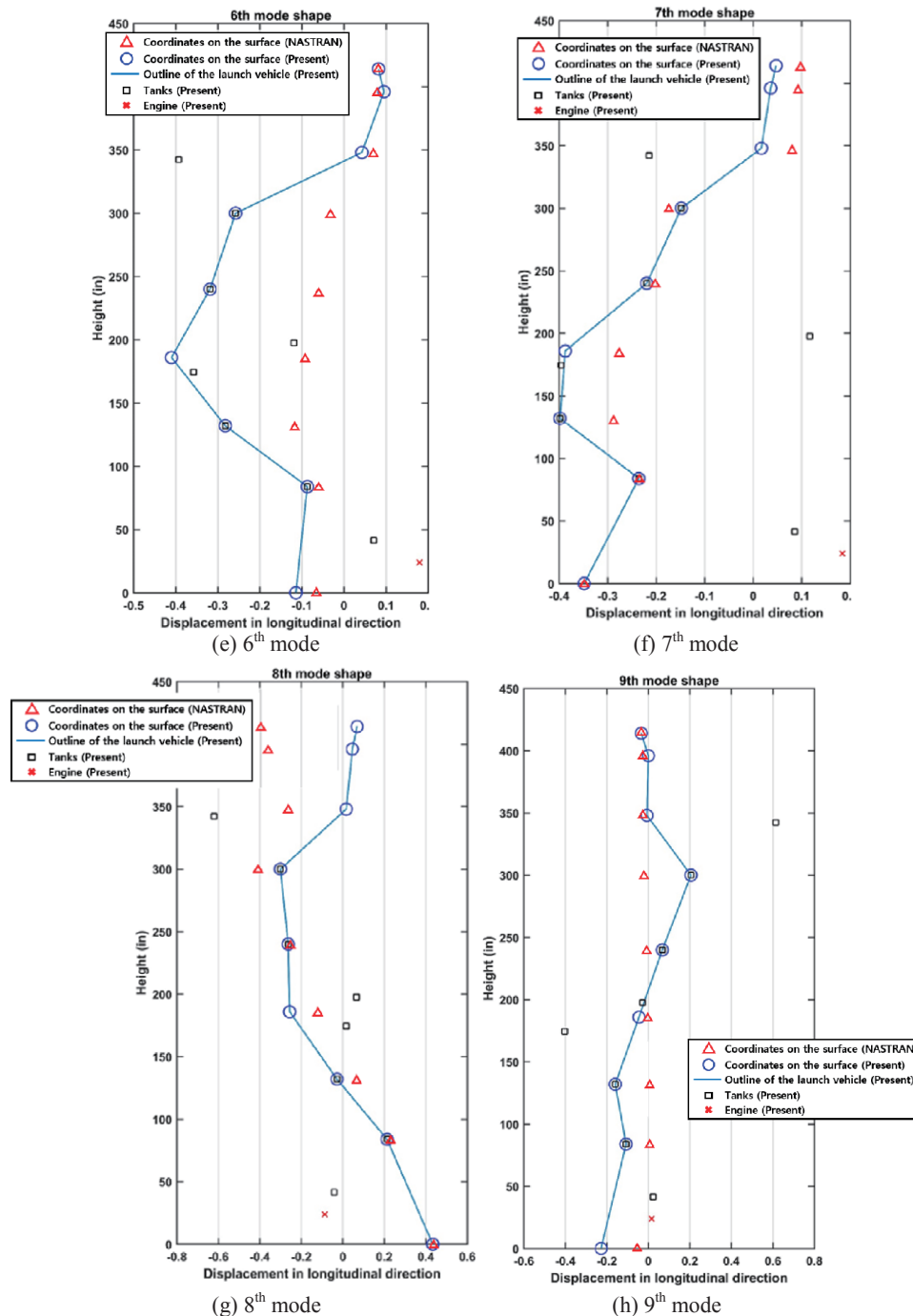


Fig. 11. Comparison of the 2nd~9th mode shapes of the example launch vehicle

Table 1. Comparison of the natural frequencies between the present and three-dimensional NASTRAN analysis

Mode	Natural frequencies by the present analysis (Hz)	Natural frequencies by 3-D NASTRAN analysis (Hz)	Difference between the present and NASTRAN (%)
1st mode	37.60	32.637	15.2
2nd	59.94	59.301	0.01
3rd	82.79	93.904	-11.8
4th	114.80	120.87	-5.02
5th	177.22	193.38	-8.35
6th	224.79	229.72	-2.14
7th	289.89	271.16	6.91
8th	376.16	382.24	-1.01
9th	450.34	459.26	-1.94

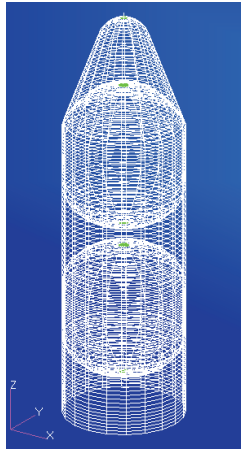


Fig. 12. NASTRAN three-dimensional analysis configuration

5. Conclusion

This paper suggests and develops an improved methodology for the pogo phenomenon. Previous researchers dealt with various launch vehicles in Europe and Asia as well as some in the U.S. Accurate predictions are required for the pogo phenomenon in a liquid-propellant launch vehicle. This paper focused on the structural modeling and on a modal analysis of a liquid-propellant launch vehicle. Specifically, the transfer function $G(s)$ was estimated to develop the pogo analysis. The formulation and analysis were developed using an approach which relied on a two-dimensional axisymmetric shell element. The present analysis was validated in comparison with three-dimensional NASTRAN prediction results. The present methodology using the axisymmetric shell element adopted the Rayleigh-Ritz method. In this methodology, a liquid-propellant launch vehicle was divided into the following three components: the spring-mass, the shell, and the fluid components. The present shell element differed from that

used in the general finite element method. Furthermore, the fluid component did not generate additional degrees of freedom. In more detail, the present numerical integration was conducted using a variable step size instead of the 16-point Gaussian weighting methodology in order to improve the accuracy.

Furthermore, the axial frequency predictions by the present analysis were compared with the three-dimensional NASTRAN analysis results. Both results yielded consistent natural frequencies and mode shapes for the example launch vehicle. The present analysis has an advantage in terms of computational resource usage because it uses far fewer degrees of freedom when compared with the three-dimensional analysis.

In the future, several ideas will be added to the proposed methodology in order to extract more accurate dynamic characteristics of a launch vehicle. First, when the degrees of freedom of the present shell element are expanded to those for three dimensions, detailed launch vehicle characteristics such as bending and breathing modes will be available as well as the longitudinal modes. These can be used to predict instability of the launch vehicle, including the pogo phenomenon, more accurately. Second, when the complex internal components of the launch vehicle are modeled as simple shell elements based on experimental results, a modal analysis can be conducted without requiring a large number of degrees of freedom, as required in a three-dimensional full-scale finite element computation. This will greatly improve the computational efficiency of the analysis.

On the other hand, other launch vehicles can also be analyzed using the methodology proposed here. Finally, these results can be used to create a pogo analysis. The chances of the natural frequencies overlapping with those of the feedlines and the propulsion system can also be estimated.

Acknowledgement

This work was supported by the Advanced Research Center Program (NRF-2013R1A5A1073861) through a grant from the National Research Foundation of Korea (NRF) funded by the Korean government (MSIP) through a contract with the Advanced Space Propulsion Research Center at Seoul National University.

Nomenclature

P_s	= Propellant force
E	= Thrust gain
f	= Disturbance force
K_s	= Cavitation stiffness of a pump inlet
D_s	= Orifice effect of a pump
m_s	= Lox mass
m	= Structure mass
$[M]$	= Mass matrix
$[K]$	= Stiffness matrix
ω_n	= Natural frequency
$[\phi]$	= Mode shape vector
$u[\xi]$	= Displacement of the shell component in the longitudinal direction
$v[\xi]$	= Displacement of the shell component in the radial direction
ξ	= Dimensionless variable for the shell element
C_{11}, C_{12}, C_{22}	= Orthotropic stress-strain coefficients
C_{33}, C_{34}, C_{44}	= Orthotropic moment-curvature coefficients
t	= Thickness of the shell
γ_a	= Density of the shell
γ_b	= Density of the fluid
x	= Coordinate in the longitudinal direction
r	= Coordinate in the radial direction

References

[1] Ryan, S. G., "Vibration Challenges in the Design of NASA's Ares Launch Vehicles", *2009 International Design Engineering Technical Conference: 22nd Biennial Conference on Mechanical Vibration and Noise*, San Diego, CA, Aug. 30 - Sep. 2, 2009.

[2] Larsen, C. E., "NASA Experience with Pogo in Human Spaceflight Vehicles", *NATO RTO Symposium ATV-152 on Limit-Cycle Oscillations and Other Amplitude-Limited, Self-Excited Vibrations*, Norway, May 5-8, 2008.

[3] Rubin, S., "Longitudinal Instability of Liquid Rockets Due to Propulsion Feedback (POGO)", *Journal of Spacecraft*,

Vol. 3, No. 8, 1966, pp. 1188-1195.

[4] Oppenheim, B. W. and Rubin, S., "Advanced Pogo Stability Analysis for Liquid Rockets", *Journal of Spacecraft and Rockets*, Vol. 30, No.3, 1993, pp. 360-373.

[5] Payne, J. G. and Rubin, S., "Pogo Suppression on the Delta Vehicle", AD-784833, 1974.

[6] Sterett, J. B. and Riley, G. E., "Saturn V/Apollo Vehicle Pogo Stability Problems and Solutions", *AIAA 7th Annual Meeting and Technological Display*, Houston, TX, Oct. 19-22, 1970.

[7] von Pragenau, G. L., "Stability Analysis of Apollo-Saturn V Propulsion and Structure Feedback Loop", *AIAA Guidance, Control, and Flight Mechanics Conference*, New Jersey, NJ, Aug. 18-20, 1969.

[8] Doiron, H. H., "Space Shuttle Pogo Prevention", *Society of Automotive Engineers Aerospace Meeting*, Los Angeles, CA, Nov. 14-17, 1977.

[9] Lock, M. H. and Rubin, S., "Passive Suppression of Pogo on the Space Shuttle", NASA CR-132452, 1974.

[10] Swanson, L. and Giel, T., "Design Analysis of the Ares I Pogo Accumulator", *45th AIAA/ASME/SAE/ASEE Joint Propulsion Conference & Exhibit*, Denver, CO, Aug. 2-5, 2009.

[11] Anonymous, "NASA Space Vehicle Design Criteria-Prevention of Coupled Structure-Propulsion Instability (POGO)", NASA SP-8055, 1970.

[12] About, G., Bouveret, P. and Bonnal, C., "A New Approach of Pogo Phenomenon Three-Dimensional Studies on the Ariane 4 Launcher", *Acta Astronautica*, Vol. 15, Issues 6-7, 1987, pp. 321-330.

[13] Ujino, T., Morino, Y., Kohsetsu, Y., Mori, T. and Shirai, Y., "POGO Analysis on the H-II Launch Vehicle", *30th Structures, Structural Dynamics and Materials Conference*, Mobile, AL, April 3-5, 1989.

[14] Zhao, Z. and Ren, G., "Parameter Study on Pogo Stability of Liquid Rockets", *Journal of Spacecraft and Rockets*, Vol. 48, No. 3, 2011, pp. 537-541.

[15] Hao, Y., Tang, G. and Xu, D., "Finite-Element Modeling and Frequency-Domain Analysis of Liquid-Propulsion Launch Vehicle", *AIAA Journal*, Vol. 53, No. 11, 2015.

[16] Chang, H. S., "A Study on the Analysis of Pogo and its Suppression", *Master's Thesis*, Korea Advanced Institute of Science and Technology, Department of Mechanical Engineering, 2002.

[17] Pinson, L. D., "Longitudinal Spring Constants for liquid-Propellant Tanks with Ellipsoidal Ends", NASA TN D-2220, 1964.

[18] Pengelley, C. D., "Natural Frequency of Longitudinal Modes of Liquid Propellant Space Launch Vehicles", *Journal of Spacecraft*, Vol. 5, No. 12, 1968, pp. 1425-1431.

[19] Anonymous, "NASA Space Vehicle Design Criteria-Natural Vibration Modal Analysis", NASA SP-8012, 1970.

- [20] Anonymous, "NASA Space Vehicle Design Criteria-Structural Vibration Prediction", NASA SP-8050, 1970.
- [21] Kim, J., Sim, J., Shin, S., Park, J. and Kim, Y., "Advanced One-dimensional Dynamic Analysis Methodology for Space Launch Vehicles Reflecting Liquid Components", *Aeronautical Journal*, in revision.
- [22] Archer, J. S. and Rubin, C. P., "Improved Analytic Longitudinal Response Analysis for Axisymmetric Launch Vehicle", Vol. 1, NASA CR-345, 1965.
- [23] Rubin, C. P. and Wang, T. T., "Improved Analytic Longitudinal Response Analysis for Axisymmetric Launch Vehicle", Vol. 2, NASA CR-346, 1965.
- [24] Pinson, L. D. and Leadbetter, S. A., "Some Results from 1/8-Scale Shuttle Model Vibration Studies", *Journal of Spacecraft*, Vol. 61, No. 1, 1979.
- [25] Sim, J., Kim, J., Lee, S., Shin, S., Choi, H. and Yoon, W., "Further Extended Structural Modeling and Modal Analysis of Liquid-Propellant Launch Vehicles for Pogo Analysis", *AIAA SPACE Conference and Exposition*, Long Beach, NJ, Sep. 13-16, 2016.
- [26] Sim, J., "Structural Dynamic Analysis of Space Launch Vehicle Using Axisymmetric Shell Element Including Hydroelastic Effect for Pogo Stability Analysis", *Master's Thesis*, Seoul National University, 2017.